



Growth mechanism of graphite-carbon encapsulated nickel catalysts and curvature effect of carbon layer on the performance of catalytic hydrogenation



Wei He, Jiaxin Yu, Xiyuan Zhang, Yebin Zhou, Yongyue Yao, Chaofan Ma, Chunyu Yin, Wei Yan, Yi Liu ^{*}, Chunshan Lu ^{*}, Xiaonian Li ^{*}

State Key Laboratory Breeding Base of Green Chemistry Synthesis Technology, Zhejiang University of Technology, Hangzhou 310032, People's Republic of China

ARTICLE INFO

Keywords:

Pyrolysis
Encapsulated catalyst
Curvature
Nitro hydrogenation

ABSTRACT

This research focuses on the growth mechanism from organometallic coordination polymers precursor to encapsulated catalyst, which contributes to the guiding for the directional design and controlled preparation of the catalyst. Decomposition of organic matter, reduction of nickel, and dissolution/segregation of carbon in the nickel nanoparticles are three main steps for the conversion of Ni@C-OCPs to Ni@C under pyrolysis. The contents of reducing atmosphere during pyrolysis were reduced via selecting organic ligands with smaller molecular and higher C-H ratios. Thus, Ni@C-600 with smaller particle size and larger curvature of the carbon layer surface was obtained. Kinetic experiments showed that it corresponded to a lower apparent activation energy. In addition, density function theory simulation verified that the optimization of the electronic structure generated by the large curvature graphite carbon layer was one of the sources of its excellent activity.

1. Introduction

In recent years, metal catalysts are facing critical challenges to cope with the development of new green chemistry [1,2], such as surviving in highly acidic, alkaline, or toxic environments [3,4]. Confronted with these issues, it is extremely difficult to develop efficient and environmentally friendly catalytic reaction paths in some fields. For example, substitution aniline is an important intermediate product and applied in the fine chemical industry including pigments, dyes, agrochemicals, pharmaceuticals, liquid crystals, and polymer materials [5–8]. However, in the process of hydrogenation of halogenated nitrobenzene to halogenated aniline, it is hard to be implemented in large-scale catalytic production due to metal leaching and catalyst poisoning, which are caused by the side reactions of dehalogenation and the reagent purity in industrial production, respectively [9]. Thus, traditional chemical synthesis methods with complex steps and low atom utilization are still wildly used. The stoichiometric reduction technology of extracting aniline from nitrobenzene with base metal as a reducing agent in an acidic medium is still the main method for producing substituted aniline [2, 10]. The traditional process with low production efficiency, poor economic benefits, and large environmental pollution is difficult to meet the

production requirements of substitution anilines in the new era. Therefore, it is necessary and urgent to intensify the viability and stability of metal catalysts in extreme conditions in the catalytic hydrogenation process.

A novel and promising strategy are proposed to encapsulate the transition metals (TMs) with the carbon layer [11,12]. The stability of the catalyst under extremely harsh conditions can be ensured by the carbon layer completely isolating the external reaction environment from TMs. The occurrence of a catalytic reaction can be ensured via the interaction between the carbon layer and the TMs core. Although the encapsulation of thick carbon layers provides a longer service life for the TMs core, usually reduces the catalytic activity [13]. Single-layer encapsulation will indeed bring higher catalytic activity, corresponding to the decline of its chemical stability [14]. How to maintain high stability while possess excellent catalytic activity is one of eternal propositions for researchers. Ito et al. [15] achieved a balance between stability and activity by controlling the number of carbon layers. Shen et al. [16] promoted the activity by introducing heteroatomic nitrogen in carbon layers. Similarly, the functional groups of the carbon layer and the particle size of the encapsulated metal core can affect the catalytic activity [17,18]. However, the effect of curving the graphene framework

* Corresponding authors.

E-mail addresses: yiliu@zjut.edu.cn (Y. Liu), lcsjcn@zjut.edu.cn (C. Lu), xnli@zjut.edu.cn (X. Li).

has been ignored when the carbon layer encapsulates TMs. The π -orbital belonging to carbon is initially perpendicular to the graphene-carbon layer, which induces the material to rehybridize due to its curvature characteristics, and forms a mixture between the sp^2 and sp^3 orbitals [19–21]. Therefore, the electron transformation process and the electron distribution on the surface of the curve graphene are different from graphite plane [11,22]. Thus, regulation of the carbon layer curvature to obtain the special electronic structure is one of the keys to ensuring the high activity and stability of the catalyst.

To date, there are a variety of synthetic routes for graphene-encapsulated metal catalysts, including chemical vapor deposition (CVD), in situ growth, arc discharge method, high-temperature pyrolysis, etc. [23,24]. Direct pyrolysis of organometallic coordination polymers (OCP) has become one of the most effective methods to prepare carbon encapsulating catalysts due to its low cost, controllable process, and simple method [25–27]. OCP precursor as input, metal cations and organic ligands were selected for coordination optimization. And catalysts as output, how to improve the catalytic performance. These are the focus of researchers. However, pyrolysis, one of the most important steps in the preparation process, is still unknown as a black box. The investigation of the pyrolysis step allows us to understand how the precursor is mechanically transformed during pyrolysis and how it converts to the special structure of graphene-encapsulated TMs. It will provide a new approach for the directional design and controllable preparation of graphite-carbon encapsulated TMs catalyst.

In this work, we provide a method for preparing encapsulated TMs@C catalysts by high-temperature pyrolysis of OCP precursors. TG, MS, XRD, Raman, XAFS and other characterization methods were used to reveal the mechanical transformation from precursor to catalyst during pyrolysis. The growth mechanism of graphitization catalyzed by the carbon layer in the catalyst was also proposed and confirmed. Through the selection of organic ligands, we regulated the pyrolysis process and prepared a catalyst Ni@C-600 with a smaller particle size and larger curvature carbon layer. Further kinetic experiments showed that Ni@C-600 has a faster reaction rate and lower apparent activation energy. Density function theory (DFT) simulation predicted that the high catalytic activity of Ni@C-600 is largely due to the better electronic structure from its large curvature carbon layer. Also, the Ni@C-600 catalyst possesses excellent catalytic efficiency for selective hydrogenation of p-chloronitrobenzene to p-chloroaniline with excellent recyclability, stability, broad sulfur resistance, and substrate potential.

2. Experimental section

The specific details of chemicals and agents, physical characterization, and DFT simulations are reflected in the [supporting information](#).

2.1. Synthesis of samples

For Ni@C-600, 0.5 g succinic acid and 1.8 g $Ni(NO_3)_2 \cdot 6 H_2O$ were added into a mixed solution of 75 mL N, N-Dimethylformamide (DMF), and 75 mL absolute ethanol in a 250 mL glass beaker. After the material was completely dissolved at 60 °C, 3 mL $NH_3 \cdot H_2O$ was added and stirred continuously for 6 h. After being stirred at room temperature for 12 h and filtered, washed, and dried, the Sample Ni@C-OCPs were collected. Finally, the Ni@C-600 were calcined at 600 °C for 300 min (heating rate of 1 °C·min⁻¹) at N_2 atmosphere. For Ni@C-1, the organic ligand was replaced with 0.7 g of terephthalic acid. Other preparation methods are the same as above. All catalysts were washed in 1 M H_2SO_4 solution for 5 h. The as-prepared Ni@C-OCPs powder was annealed at 200–550 °C at N_2 atmosphere for 300 min, and Ni@C-200, Ni@C-300, Ni@C-350, Ni@C-400, Ni@C-450, Ni@C-500, and Ni@C-550, respectively, were finally fabricated.

2.2. Catalytic hydrogenation tests

Using the hydrogenation reaction of nitrobenzene derivatives as probe reaction (hydrogen as reducing agent), the performance of each catalyst was studied. The experiment was conducted in a 50 mL stainless steel autoclave. Before each reaction, purged with H_2 five times to replace the air in the reactor. The reaction was analyzed by gas chromatography (Agilent 7890 A), FID detector, and HP-5 capillary column (30 m × 0.20 mm × 0.25 μ m), and area normalization method.

3. Results and discussion

3.1. Synthesis and characterizations of Ni@C-OCPs

Succinic acid is the carboxylic acid organic ligand with no specificity for chelating metal cations [28,29]. Ammonia was used as the deprotonation reagent to accelerate the chelation of succinic acid and $Ni(NO_3)_2 \cdot 6 H_2O$ to form Ni@C-OCPs. As identified by the SEM images (Fig. 1a), the porous and irregular 3D hierarchical structure is synthesized. According to the EDX elemental mappings, the three elements C, O, and Ni are uniformly distributed on the Ni@C-OCPs structure (Fig. s1). FT-IR spectroscopy can be used to further understand Ni@C-OCPs, as shown in Fig. 1b. In the spectra of Ni@C-OCPs, compared with the spectra of free succinic acid, the band at 1700 cm^{-1} corresponding to the C=O stretching vibration of the carboxylate group disappears [30]. However, two strong adsorption bands appear at 1579 and 1390 cm^{-1} , corresponding to symmetric and asymmetric vibrations of COO- groups [31,32]. These all indicate succinic acid was completely deprotonated by ammonia and chelated with Ni^{2+} to form Ni@C-OCPs. Through the XRD of Ni@C-OCPs (Fig. s2), it can be found that there are many sharp peaks in the range of 10–30°, indicating the formation of its crystal structure, and can be mutually confirmed with the above conclusion [33,34].

3.2. Transformed mechanism of Ni@OCPs to Ni@C

TGA curves were used to study the thermal behavior of Ni@C-OCPs during pyrolysis (Fig. 2a). It can be divided into three regions of mass loss and two large intervals of heat change (upward is endothermic, downward is exothermic). The first mass loss interval is between 83 and 215 °C, corresponding to a 21% mass loss and a large heat absorption interval. According to the MS signal under the same pyrolysis conditions (Fig. 2b), CH_4 , H_2O , and a small amount of C_2H_4 escaped from Ni@C-OCPs in this temperature segment. Therefore, it can be inferred that at the beginning of the pyrolysis process, the free water, and bound water molecules on Ni@C-OCPs surface will begin endothermic evaporation [35]. At the same time, some unstable carbon skeletons in the precursor would be thermally decomposed to form CH_4 and a few C_2H_4 . The second weight loss (215–363 °C, 26% mass loss) and the third weight loss (363–507 °C, 36% mass loss) interval corresponded to a large exothermic phase. Moreover, CO , $EtOH$, C_2H_4 , CO_2 , H_2O , and CH_4 appeared on the mass spectrogram. As a result, the two weight loss intervals correspond to the evaporation of a small number of solvent molecules (EtOH) and the exothermic decomposition of more unstable carbon chain skeletons, respectively [36]. It is worth noting that the reducing gas C_2H_4 and CO is produced, and H_2O is still generated at high temperatures (between 350 and 450 °C). In addition, an exothermic thermal behavior also occurred. This may be related to the redox reaction during Ni@C-OCPs pyrolysis.

Further phase changes can be received from the XRD patterns of Ni@C-x (Fig. 2c). With the increase in temperature (room temperature–300 °C), the sharp peak (10°–30°) originally belonging to Ni@C-OCPs gradually disappeared. And, it converted into a large packet peak (belonging to an amorphous carbon) [37]. This indicates that the crystal structure of OCPs is destroyed, the carbonization process begins, and the OCPs are transformed into amorphous carbon. This may be related to the

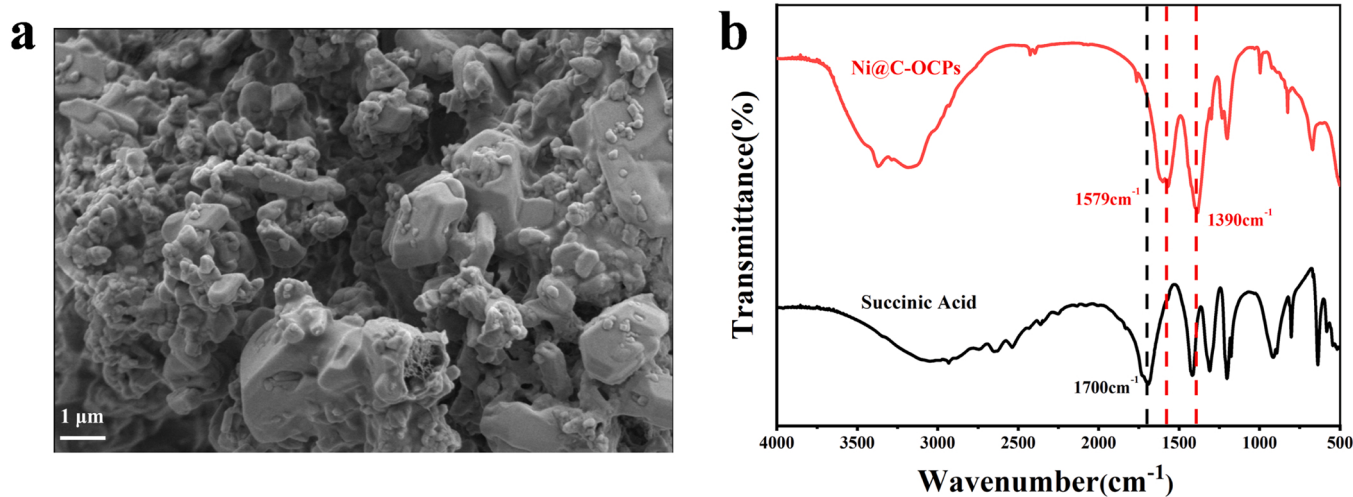


Fig. 1. (a) SEM image of Ni@C-OCPs; (b) FT-IR spectra of Ni@C-OCPs and Succinic Acid.

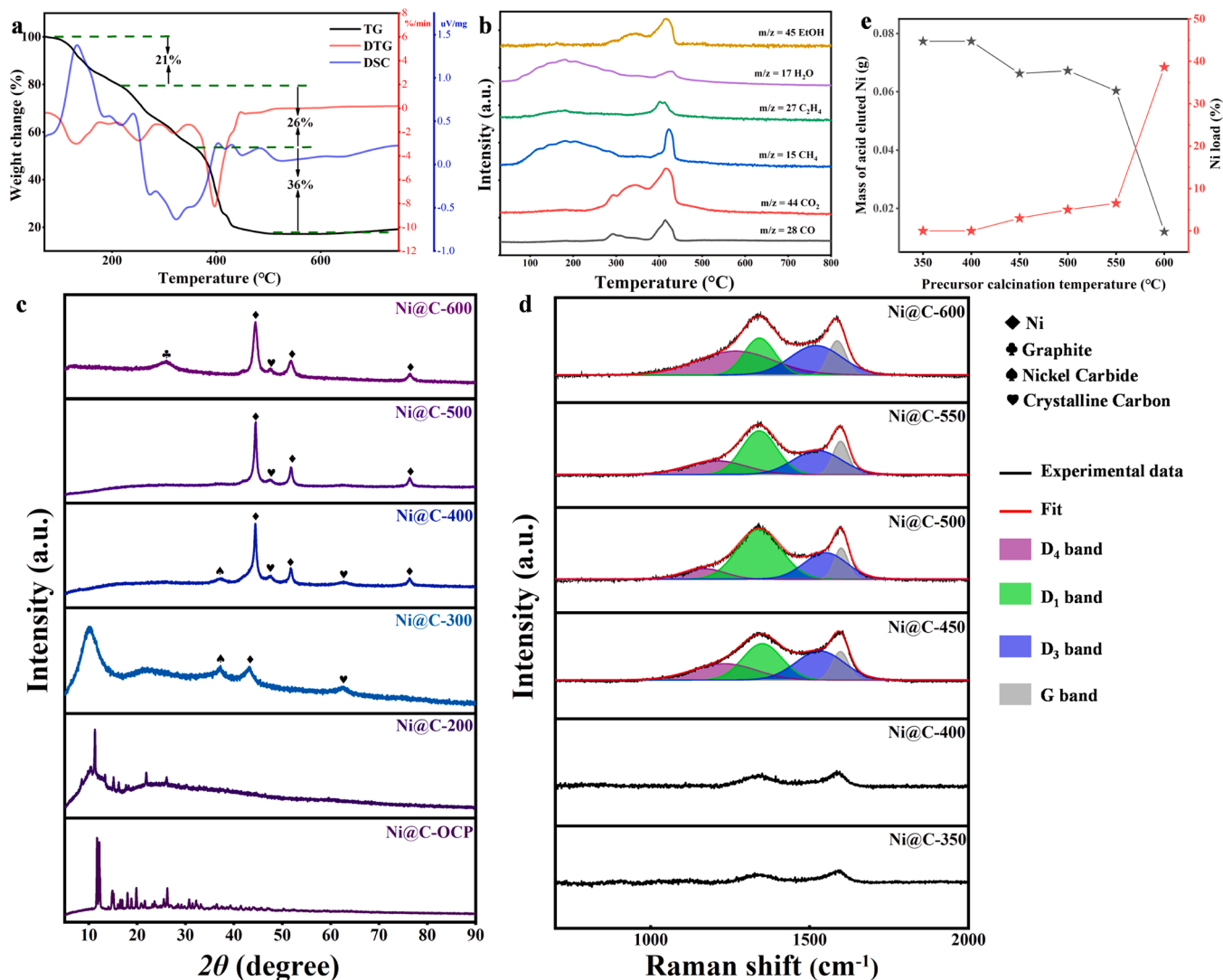


Fig. 2. (a) Thermogravimetric analysis (TGA) and (b) Mass spectrum (MS) curves of Ni@C-OCPs measured in Helium at a heating rate of $10^{\circ}\text{C} \cdot \text{min}^{-1}$; (c) XRD patterns and (d) Raman spectra of Ni@C-OCPs at different calcination temperatures; (e) Different roasting temperature Ni@C-OCPs, metal load after pickling and nickel content removed by pickling. conditions: 1 M H_2SO_4 solution at 600 rpm for 5 h.

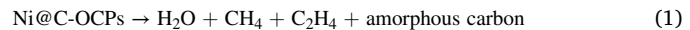
decomposition of the unstable carbon chain skeleton mentioned before. In the XRD pattern of the Ni@C-300 sample, three diffraction peaks positioned at 37.1, 43.2, and 62.4° are well-indexed to Nickel Carbide (PDF#70-1849), Ni (PDF#70-1849), and Crystalline Carbon (PDF#80-0004), respectively[38]. Significantly, the metallic nickel peak position at Ni@C-300 has a lower angular shift compared to the diffraction peak at 44.5° of the standard nickel phases. It is possible that some of the carbon atoms dissolve into the Ni nanoparticles, or that some of the carbon atoms mix with the Ni atoms[39–42]. However, the appearance of two phases, Nickel Carbide and Crystalline Carbon can be associated with the catalytic graphitization of nickel metal, proving that the cause is not simply physical mixing[41]. Crystalline Carbon is a transition state between amorphous carbon and graphite carbon[43]. Nickel Carbide (Ni₃C) is formed through the combination of metallic Ni and amorphous carbon. With the further increase in pyrolysis temperature (400–600 °C), the deviation of the diffraction peak of the nickel crystal phase disappeared, and nickel carbide and the large packet peak at 10°–30° gradually disappeared. In the meantime, the diffraction peaks positioned at 44.5, 51.8, and 76.5° were well-indexed to (111), (200), and (220) planes of the Ni phase (PDF#70-1849), and the peaks at 47.3 and 62.3° were attributed to the (101) and (102) crystal face of the Crystalline Carbon (PDF#80-0004). In addition, a diffraction peak (26°) belonging to the graphitic carbon (002) crystal plane appeared on the XRD pattern of Ni@C-600[42]. These phase changes indicate that an OCP precursor can be slowly transformed into a composite of nickel nanoparticles and graphite-carbon with the pyrolysis process.

Further, an investigation of the formation mechanism of graphite carbon could be acquired from the Raman spectrum of Ni@C-x (Fig. 2d). Starting from about 350 °C, with the increase of pyrolysis temperature, the two bands exclusively for carbon materials in the sample became more and more obvious, indicating that the degree of carbonization is also increasing. To get more detailed information from Raman spectra, Ni@C-450, Ni@C-500, Ni@C-550, and Ni@C-600 spectrum was subjected to peak fitting using a curve fitting software, Origin8.0/Peak Fitting Module, to resolved curve into 4 Gaussian bands. In the Raman spectra of carbonaceous materials, the band at about 1600 cm⁻¹ is called the G band, corresponding to perfect graphene without defects. The 1350 cm⁻¹ band is commonly called the D₁ band (one of the defect bands), attributed to the in-plane imperfections in graphite such as defects and heteroatoms. The generally appears as a very broad band around 1500–1550 cm⁻¹ (D₃ band), suggests to originate from the amorphous sp²-bonded forms of carbon, and usually manifests itself as fragments, organic molecules, or functional groups. The D₄ band (about 1200 cm⁻¹ band) appears only in very poorly organized materials, such as coal chars and soot[44–46]. The Raman spectral properties, such as the intensity ratio of the D₁ band and G band have been proven to have good correlations with the degree of carbon structural order[47]. The I_G/I_{D1} ratios of Ni@C-450, Ni@C-500, Ni@C-550, and Ni@C-600 samples corresponded to 0.68, 0.70, 0.84, and 0.93, respectively. The result shows that the increase in pyrolysis temperature is beneficial to the increase of the graphitization degree of the carbon layer in the catalyst. In addition, as shown in Table s1, the higher the degree of graphitization of the carbon layer, the better the hydrogenation activity of the catalyst. Due to its better interaction with the inner metal core, it can obtain more electrons and has stronger reactivity.

The degree of graphitization of the carbon layer could be further illustrated by comparing the metal loading of these samples after pickling and the content of nickel removed by pickling (Fig. 2e). After pickling with 1 M H₂SO₄ solution for 5 h, the nickel load of the sample with a lower graphitization degree was lower, and the nickel content in the acid lotion was higher (Ni@C-350, Ni@C-400, Ni@C-450, Ni@C-500, and Ni@C-550). The most graphitized Ni@C-600 retained 34% nickel content and almost no nickel was leached in the acid wash. This indicates that the nickel core inside is effectively isolated from the outside environment by the highly graphitized carbon layer. The regularity between the degree of graphitization and pyrolysis temperature

may be related to the catalytic graphitization of the transition metal nickel[39,40,42].

Based on the above analysis, it can be accurately obtained the transformed mechanism of Ni@OCPs to Ni@C-600. It can be separated into three steps: decomposition of organic matter, reduction of Ni, and dissolution/segregation of carbon in the Ni nanoparticles. Firstly, in the initial heating stage (<300 °C), the carbonization process of Ni@C-OCPs begins, and some adsorbed water molecules and unstable carbon chain skeletons begin to dehydrate and decompose, respectively. And the original crystal structure is transformed into an amorphous carbon structure.



Secondly, in the mesothermal stage (300–400 °C), the more stable carbon chain skeleton in Ni@C-OCPs (Ni@C-OCPs*) also begins to undergo thermal decomposition, releasing some reducing gases (C₂H₄ and CO), CH₄, and CO₂. At the same time, the Ni²⁺ which is originally coordinated with the carboxyl group of succinic acid is reduced to Ni by some reducing component. Furthermore, the combination of metal Ni and amorphous carbon forms Nickel Carbide (Ni₃C). Finally, with the increase of pyrolysis temperature, Ni₃C is decomposed into Ni and crystalline carbon. When the temperature rises to 600 °C, the crystalline carbon is transformed into graphite carbon. And the unique structure of graphite carbon encapsulated nickel metal core is formed.

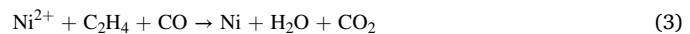
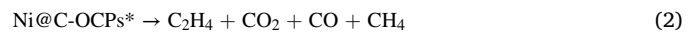


Fig. 3a shows the preparation flow chart of Ni@C-OCPs, and the reaction mechanism diagram of the catalyst Ni@C-600 produced from three steps of pyrolysis. Fig. 3b is the resultant Ni@C-OCPs SEM image. Fig. 3c is the SEM image after the Ni@C-OCPs precursor underwent the first step of pyrolysis, the decomposition of the unstable carbon chain skeleton. Compared with Fig. 3b, Ni@C-200 shows obvious structural shrinkage, but the general structure does not collapse. Fig. 3d shows the TEM image of Ni@C-400. It can observe obvious nickel nanoparticles, but no graphite-carbon or encapsulation structure was found. Fig. 3e shows the Ni@C-600 TEM image after carbon dissolution and segregation in the Ni nanoparticles at the third step of pyrolysis. It has an obvious graphite-carbon encased nickel core special structure.

X-ray absorption near-edge structure (XANES) and extended X-ray absorption fine structure (EXAFS) have been used to investigate the oxidation states and local coordination environments of Ni in Ni@C-OCPs, Ni@C-200, Ni@C-400, and Ni@C-600, respectively. As shown in Fig. 3f, the near-edge absorption energy of all samples is located between Ni foil and NiO, implying that the valence state of Ni in all samples is between 0 and 2⁺[48]. Meanwhile, the energy absorption curve for the Ni@C-OCPs and Ni@C-200 is closer to that of NiO, suggesting a higher fraction of Ni-O bands. This indicates that Ni species cooperate with organic ligands and only the decomposition of organic matter occurs in Ni@C-200 corresponding to the first step of the transformation mechanism. With the increase of pyrolysis temperature, the coordination structure is destroyed, and the oxidation state of Ni decreases. The energy absorption curve for the Ni@C-400 and Ni@C-600 is closer to that of Ni foil, suggesting a higher fraction of Ni-Ni bands, which indicates Ni in the sample is reduced during the pyrolysis process, corresponding to the second step in the transformed mechanism. Due to the interaction between carbon and nickel, the Ni of both is still in a low oxidation state. In addition, the energy absorption curve for the Ni@C-600 will be closer to Ni foil than Ni@C-400, suggesting with the increase of temperature, the interaction between carbon and nickel

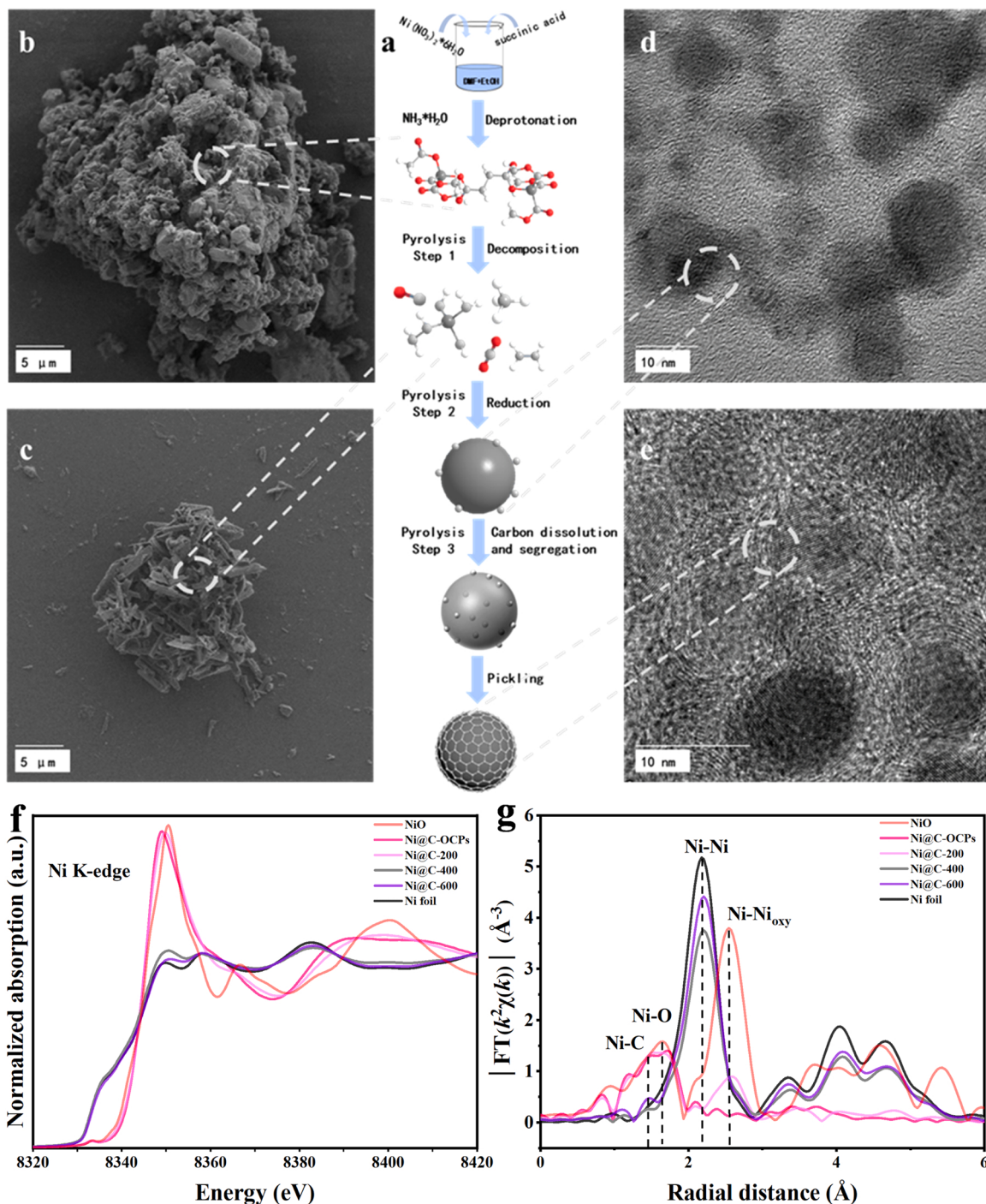


Fig. 3. (a) The flow chart of the preparation of $\text{Ni}@\text{C}$ -OCPs and the growth mechanism diagram of its pyrolysis process into $\text{Ni}@\text{C}$ -600. The gray, light gray, red, and white atoms represent Ni, C, O, and H, respectively. The corresponding electron microscope images of samples during each pyrolysis process (b) Initial sample $\text{Ni}@\text{C}$ -OCPs; (c) $\text{Ni}@\text{C}$ -200; (d) $\text{Ni}@\text{C}$ -400; (e) $\text{Ni}@\text{C}$ -600 catalyst; (f) Normalized Ni K-edge XANES spectra of NiO , $\text{Ni}@\text{C}$ -OCPs, $\text{Ni}@\text{C}$ -200, $\text{Ni}@\text{C}$ -400, $\text{Ni}@\text{C}$ -600 and Ni foil. (g) Fourier transform of the EXAFS spectra.

weakens, which corresponds to the third step dissolution/segregation of carbon in the Ni nanoparticles in the transformed mechanism. And, as shown in Fig. 3g, the EXAFS spectra for $\text{Ni}@\text{C}$ -OCPs and $\text{Ni}@\text{C}$ -200 displayed dominant Ni-O coordination with a characteristic peak at 1.64 \AA . For $\text{Ni}@\text{C}$ -400 and $\text{Ni}@\text{C}$ -600, the main peak at 2.20 \AA can be attributed to the scattering path of Ni-Ni, and the Ni-C scattering path at 1.45 \AA exists. Meanwhile, another main peak at 2.55 \AA matches well with the Ni-Ni_{oxy} backscattering path of NiO and $\text{Ni}@\text{C}$ -200[49]. These results further validate the three steps in the $\text{Ni}@\text{OCPs}$ to $\text{Ni}@\text{C}$ -600 transformed mechanism.

In conclusion, the selection of initial organic ligands would directly affect the three steps in the pyrolysis process, and then determine the structure of the catalyst. When succinic acid, an organic ligand with a smaller relative molecular mass and larger C-H ratio, was used instead of terephthalic acid, an organic ligand used by $\text{Ni}@\text{NC}$ -1. $\text{Ni}@\text{C}$ -OCPs synthesized with succinic acid as an organic ligand would produce less reducing gas when organic matter was decomposed during pyrolysis. The next step of reduction of nickel was further affected. A smaller amount of reducing agent would make the reduction of nickel inadequate and the resulting nickel nanoparticles smaller. Carbon dissolution

and segregation in small nickel nanoparticles would inevitably give rise to graphene carbon layers with greater curvature. We speculated that Ni@C-600 obtained with succinic acid as organic ligand has a smaller particle size and larger curvature of the graphene carbon layer than Ni@C-1 obtained with terephthalic acid as organic ligand.

3.3. Characterizations of Ni@C-600

The microstructure and morphology of the catalyst Ni@C-600 were observed by TEM and HRTEM. The metallic Ni NPs in the Ni@C-600 were uniformly dispersed on the entire carbon substrate (Fig. s3). The particle size of Ni NPs is mostly concentrated in the range of 6–8 nm (proportion of 33%), with an average particle size of 7.83 nm. HRTEM

images (Fig. 4a) show that the Ni NPs on the carbon base was wrapped by the carbon layer, but the shape and number of carbon layers were not orderly distributed. The number of carbon layers on the left was relatively large (4–5 layers), while the number of carbon layers on the right was relatively small (1 layer). To obtain a more detailed catalyst structure, the average value of the thickest and thinnest carbon layers was usually taken when the number of carbon layers of one sample was counted, so the number of carbon layers of most samples was 3 layers. In addition, the catalyst shape was confirmed based on the ratio of the shortest diameter (L_1) to the longest diameter (L_2) of the two-dimensional projection of each catalyst particle[50]. The closer the value of L_1/L_2 is to 1, the closer the shape of catalyst particles is to the spherical. According to statistics, the L_1/L_2 of most catalyst particles was

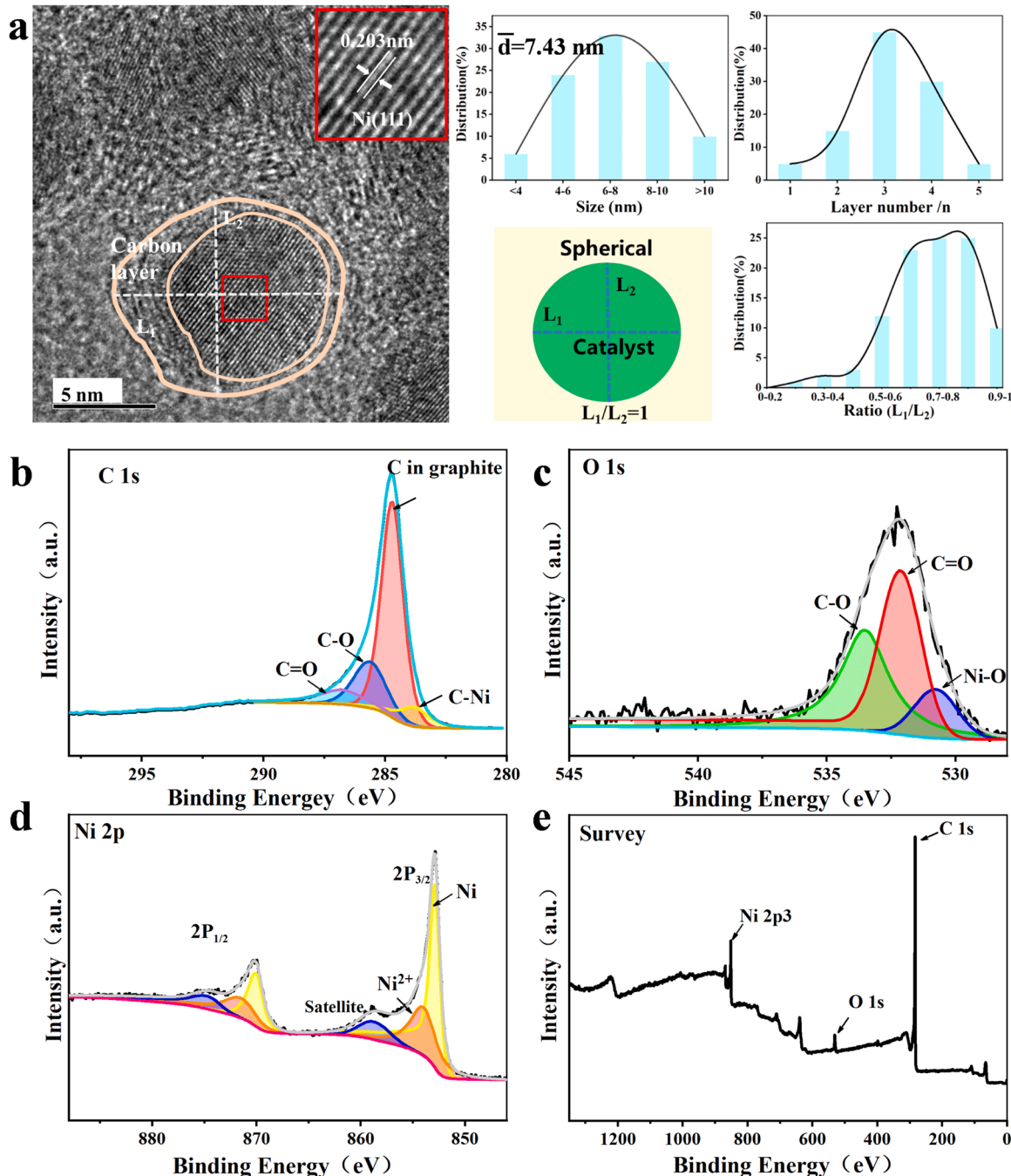


Fig. 4. (a) TEM image, Particle size distribution histogram, carbon layer number distribution histogram, and shape distribution histogram. XPS spectra of Ni@C-600 framework in (b) C 1 s; (c) O 1 s; (d) Ni 2p; (e) Survey regions.

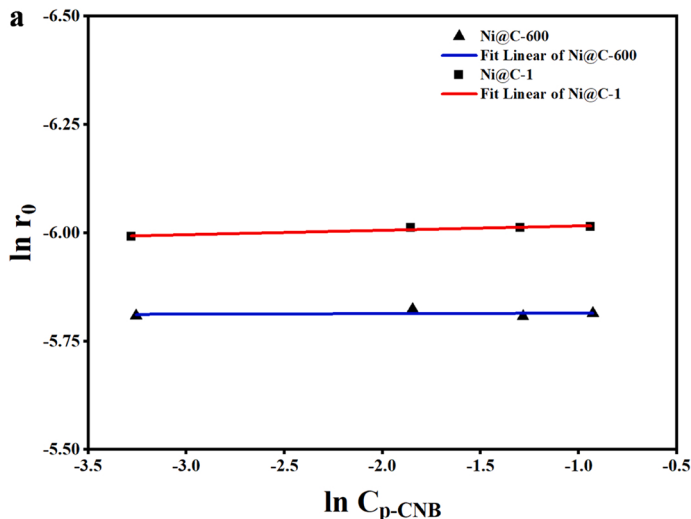
between 0.6 and 1, and the shape was close to spherical. The lattice spacing of 0.203 nm was observed, classified as the (111) crystal plane of metallic Ni [16,51]. It is further verified that the catalyst Ni@C-600 was a special structure of nickel core encapsulated by the outer graphene carbon layer.

The electronic state and surface composition of the catalyst Ni@C-600 were studied by the XPS technique. The full XPS spectrum displayed the coexistence of Ni, O, and C elements in the Ni@C-600 (Fig. 4e), consistent with the results of the element mapping (Fig. s3). The XPS survey showed that the Ni content of Ni@C-600 was only 11.84%, far from the 34% loading determined by AAS mentioned earlier (Table. s1). It is well known that XPS is a typical surface analysis method, and the sampling depth of the inorganic nonmetallic carbon layer on the surface is only 2–4 nm, while it is difficult to detect the relevant information of the internal metal core for the encapsulation structure. This further validates the formation of the sample packaging structure. The high resolution of the C 1 s spectrum was shown in Fig. 4b, it could be fitted into four bands centered at 286.8, 285.7, 284.8, and 283.8 eV corresponding to C=O, C-O, C in graphite, and C-Ni, respectively [52,53]. The High-resolution O 1 s spectrum (Fig. 4C) could be fitted into three peaks of C-O (533.5 eV), C=O (532.1 eV), and Ni-O (530.7 eV), respectively [18]. The Ni 2p XPS spectra of Ni@C-600 showed that even the surface nickel species could remain mostly metallic Ni (853.0 eV) and a small part is oxidized to Ni²⁺ (854.2 eV) [54]. The electron binding energy of metal nickel at Ni@C-600 was slightly larger than the standard metal nickel (852.8 eV). This is most likely due to the interaction between the outer carbon layer and the metal nickel core [55]. The nickel core provides electrons to the outer carbon layer, also supported by the presence of C-Ni bonds.

Through the above characterization, it was found that Ni@C-600 and Ni@C-1 (Fig. s4) have a similar structure of graphite carbon layer encapsulated nickel core. Ni@C-600 (2–4 layers shell and 7.43 nm nano-Ni core) and Ni@C-1 (1–3 layers shell and 10.21 nm nano-Ni core) have similar amounts of outer carbon layers, but the size of the encapsulated nickel cores varies. The structure of a material determines its properties. Further kinetic experiments on Ni@C-1 and Ni@C-600 were conducted to verify the difference in the performance of nitro hydrogenation due to structural differences.

3.4. Kinetic research

The apparent activation energy (E_a) of Ni@C-600 and Ni@C-1



catalysts in the hydrogenation of nitrobenzene was determined by kinetic experiments at 50 ~ 110 °C. The general rate formula for the hydrogenation of p-CNB could be expressed by Eq. (7), and more importantly, the rate formula could be further simplified to Eq. (8). Because the amount of catalyst added was constant. And the concentration of H₂ was much higher than the concentration of p-CNB, and the change over time was negligible. Eq. (9) could be differentiated from Eq. (8), and the reaction order γ of p-CNB could be obtained by making a curve of ln [p-CNB] to ln r_0 . As shown in Fig. 5a, p-CNB shows a zero-order reaction in Ni@C-600 and Ni@C-1. And Ni@C-600 shows a faster reaction rate than Ni@C-1. According to Arrhenius equation: Eq. (10), the apparent activation energy E_a could be calculated by Eq. (11).

$$r = -d_{Cp-CNB}/dt = k_0 * [Cat]^\alpha * [H_2]^\beta * [p-CNB]^\gamma \quad (7)$$

$$K = k_0 * [Cat]^\alpha * [H_2]^\beta, r = -d_{Cp-CNB}/dt = K * [p-CNB]^\gamma \quad (8)$$

$$\ln r = \ln K + \gamma * \ln [p-CNB] \quad (9)$$

$$K = A * e^{-E_a / RT} \quad (10)$$

$$\ln K = \ln A - E_a / RT \quad (11)$$

As shown in Fig. 5b, during the temperature range of 323–383 K, the apparent activation energy of Ni@C-600 is 44.09 KJ/mol, only about half that of Ni@C-1 (90.76 KJ/mol). Indicated the Ni@C-600 should represent higher catalytic activity under the same conditions [59,60]. And, compared with Ni@C-1 with an average particle size of 10.21 nm and several carbon layers of 1–3 layers, the reaction time could be shortened to 1/3 of the original under the same reaction conditions. The excellent catalytic activity demonstrated by the catalyst Ni@C-600 was astounding. However, previous studies have also shown that smaller metal nuclei lead to more optimized electronic structures, which is the source of their superior catalytic activity [17]. Typically, a more curved carbon layer corresponds to this encapsulation smaller metal core. A DFT simulation was performed to exclude the influence of the nickel core size and further obtain the direct influence of the curvature of the graphene carbon layer.

3.5. DFT simulations

In DFT simulations, the models of Ni₄ nanoparticles contained in C₆₀ ($L_1 = L_2 = 0.7115$ nm) and C₇₀ ($L_1 = 0.7105$ nm, $L_2 = 0.8291$ nm) carbon cages were constructed. Although the dimensions of the Ni

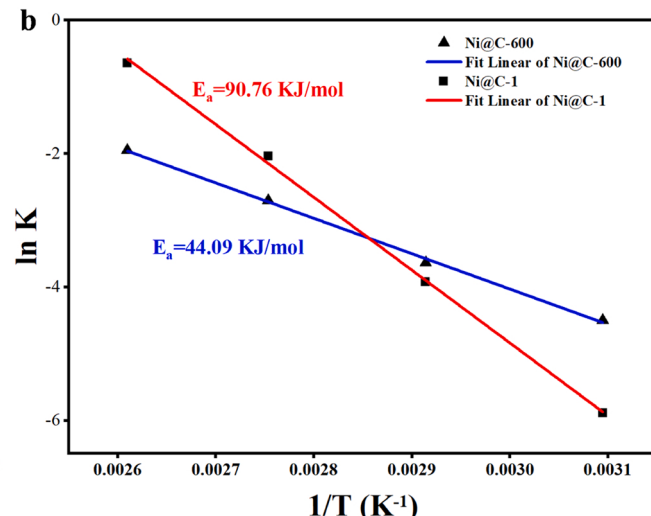


Fig. 5. (a) p-CNB concentration was used as the curve of ln r_0 against ln Cp-CNB for different initial p-CNB concentrations. Reaction conditions: 1 MPa H₂, 70 °C, 1200 rpm, initial p-CNB concentrations (mmol/mL): 0.4, 0.28, 0.16, and 0.04, solvent of methanol; (b) Ni@C-600 and Ni@C-1 Arrhenius plot in the temperature range 323.15–383.15 K. Reaction conditions: 0.02 g of the catalyst, 1.6 g of p-CNB, 25 mL of methanol, 1 MPa H₂.

nanometal core and the outer carbon layer considered in the calculations were much simpler than the experimentally observed samples. However, this simple geometry could eliminate the influence of the nickel core as much as possible, while capturing the differences in the electronic structure caused by the curvature of the carbon layer. Electron localization functions (ELFs) were used to study the electron changes caused by the curvature change of the outer carbon layer[56]. ELFs are defined as a function of values between 0 and 1, where a value of 0 (blue) indicates that the electron is completely delocalized, and a value closer to 1 (red) indicates that the electron is closer to a completely localized state[57]. As shown in Fig. 6a and b, there were distinct ionic properties between C and Ni, demonstrating charge transferred from the Ni core to the graphene carbon layer. ELFs of $C_{60}Ni_4$ (a) showed more electron localization regions in the selected plane compared to $C_{70}Ni_4$ (b) [58,59]. Through comparison of the models, it is clear that the change is entirely attributable to the size of the carbon cage structure, indicating that the curvature of the graphene carbon layer affects its electronic structure. To quantitatively assess the charge transfer of the charges in the model, we performed a Bader charge analysis[60]. As shown in Table 1, for the formal charge, 0.335 electrons were transferred from each nickel atom in $C_{60}Ni_4$ to the outer graphene carbon layer on average, while only 0.296 electrons were transferred in $C_{70}Ni_4$. For the encapsulation catalyst, electrons transfer from the nickel core to

Table 1
Calculated Bader charge analysis of $C_{60}Ni_4$ and $C_{70}Ni_4$.

Sample	Element	Initial charges	Average final charges	Total transferred charges
$C_{60}Ni_4$	C	4	4.022	+ 1.32
	Ni	10	9.665	-1.34
$C_{70}Ni_4$	C	4	4.017	+ 1.19
	Ni	10	9.704	-1.18

the outer graphene carbon layer are the source of reactivity[14,22,61]. The nickel core could transfer more electrons to the outer carbon layer with greater curvature and obtain a more optimized electronic structure.

The DFT simulation further revealed the adsorption of the reactants by the carbon layer under different curvatures. As shown in Fig. 6c, H_2 could be easily adsorbed on the surface of $C_{60}Ni_4$ (-0.02 eV). In contrast, the adsorption energy of p-CNB and H_2 on the surface of $C_{70}Ni_4$ (0.11 eV, 0.03 eV) and p-CNB on $C_{60}Ni_4$ (0.14 eV) were both positive. The results showed that the large curvature carbon layer is favorable for H_2 adsorption. To prove the effect of curvature on the whole reaction, the reaction paths of p-CNB were calculated on $C_{60}Ni_4$ and $C_{70}Ni_4$ respectively. For encapsulation catalysts, previous studies have shown that the dominant adsorption mode of the outer carbon layer is parallel

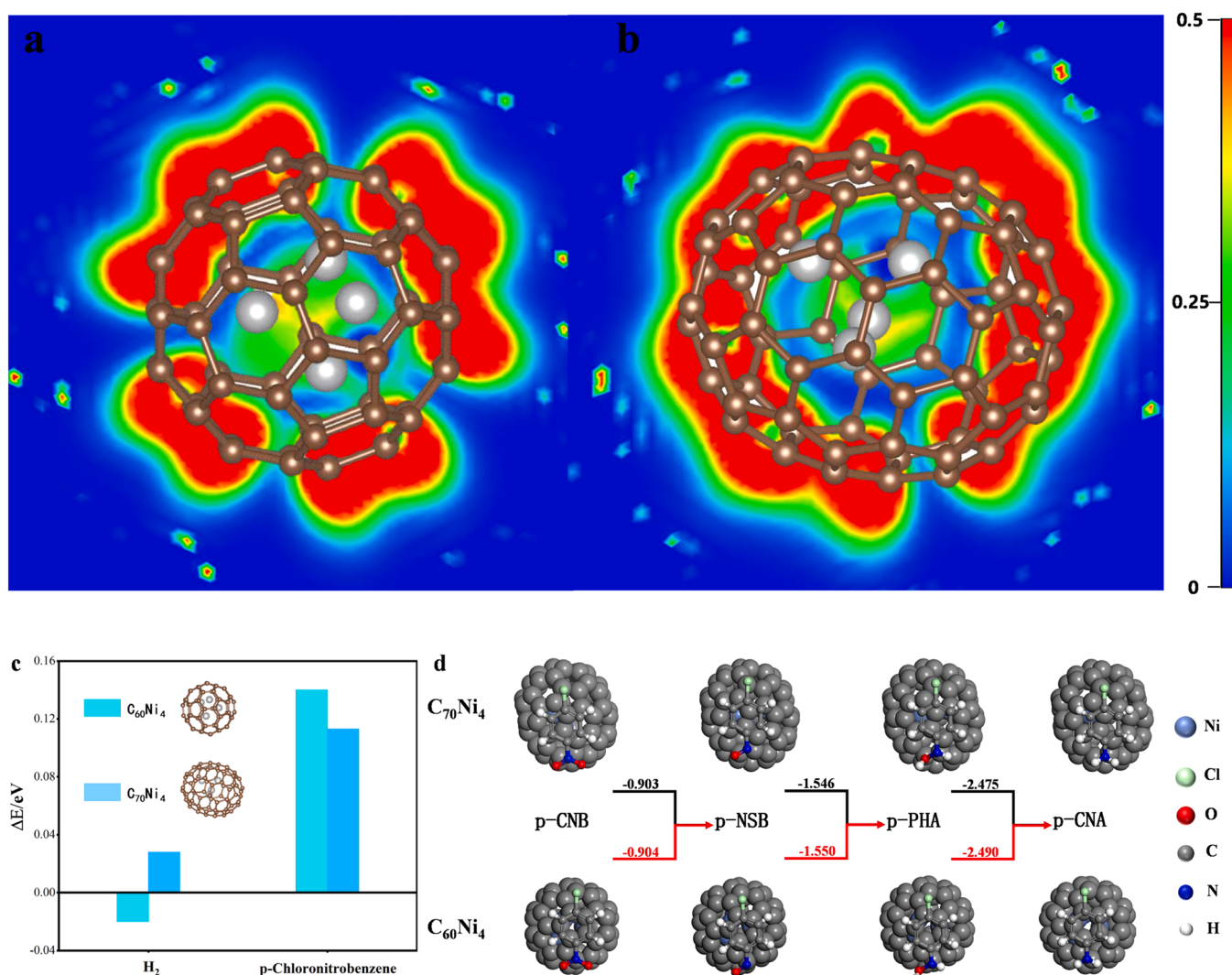


Fig. 6. Electron localization functions (ELFs) of the $C_{60}Ni_4$ (a) and $C_{70}Ni_4$ (b) catalysts from DFT calculations. The scale bar is on the right. The brown and silver atoms represent C and Ni, respectively. (c) Evaluation of adsorption energy of H_2 and p-Chloronitrobenzene on $C_{60}Ni_4$ and $C_{70}Ni_4$, respectively. (d) The reduction pathways of nitrobenzene on $C_{60}Ni_4$ and $C_{70}Ni_4$ were calculated, respectively. The values labeled near the arrows are ΔE_{ex} for each step.

adsorption. The monomolecular reaction pathway is better than the bimolecular reaction pathway. Therefore, in this study, only parallel adsorption modes and monomolecular reaction pathways were considered. As shown in Fig. 6d, the accepted Haber reaction mechanism was selected, and p-CAN was formed via p-chloronitrosobenzene (p-NSB) and p-chlorophenylhydroxylamine (p-PHA) intermediates, by the reductive transformation of the NO_2 group in p-CNB. Compared with C_{70}Ni_4 , the energy distribution shows a more optimized thermodynamic process for the hydrogenation of p-CNB to p-CNA on C_{60}Ni_4 . All the above results showed that the graphite carbon layer with large curvature is also the source of high reactivity of encapsulated catalyst, excluding the influence of encapsulated nickel core.

3.6. Catalytic performance of Ni@C-600

Unlike traditional metal catalysts, the carbon layer in the encapsulated structure can completely isolate the harsh external reaction conditions from the active metal core. In the actual industrial production process, the purity of the raw material is difficult to be guaranteed. And some sulfur impurities that cannot remove, will make the traditional metal catalyst inactive. Therefore, the sulfur resistance of catalysts is an urgent and real problem to be solved. It is also a standard to test the protection ability of the external carbon layer against the metal core. The catalyst Ni@C-600 was tested for sulfide poisoning using four different sulfur-containing poisons, including thiophene, sodium sulfide, thiourea, and potassium thiocyanate. Sulfur-containing toxicants (five times the mass of the catalyst), substrates, catalysts, etc. were added to the high-pressure reactor for reaction. As shown in Fig. 7a, under these

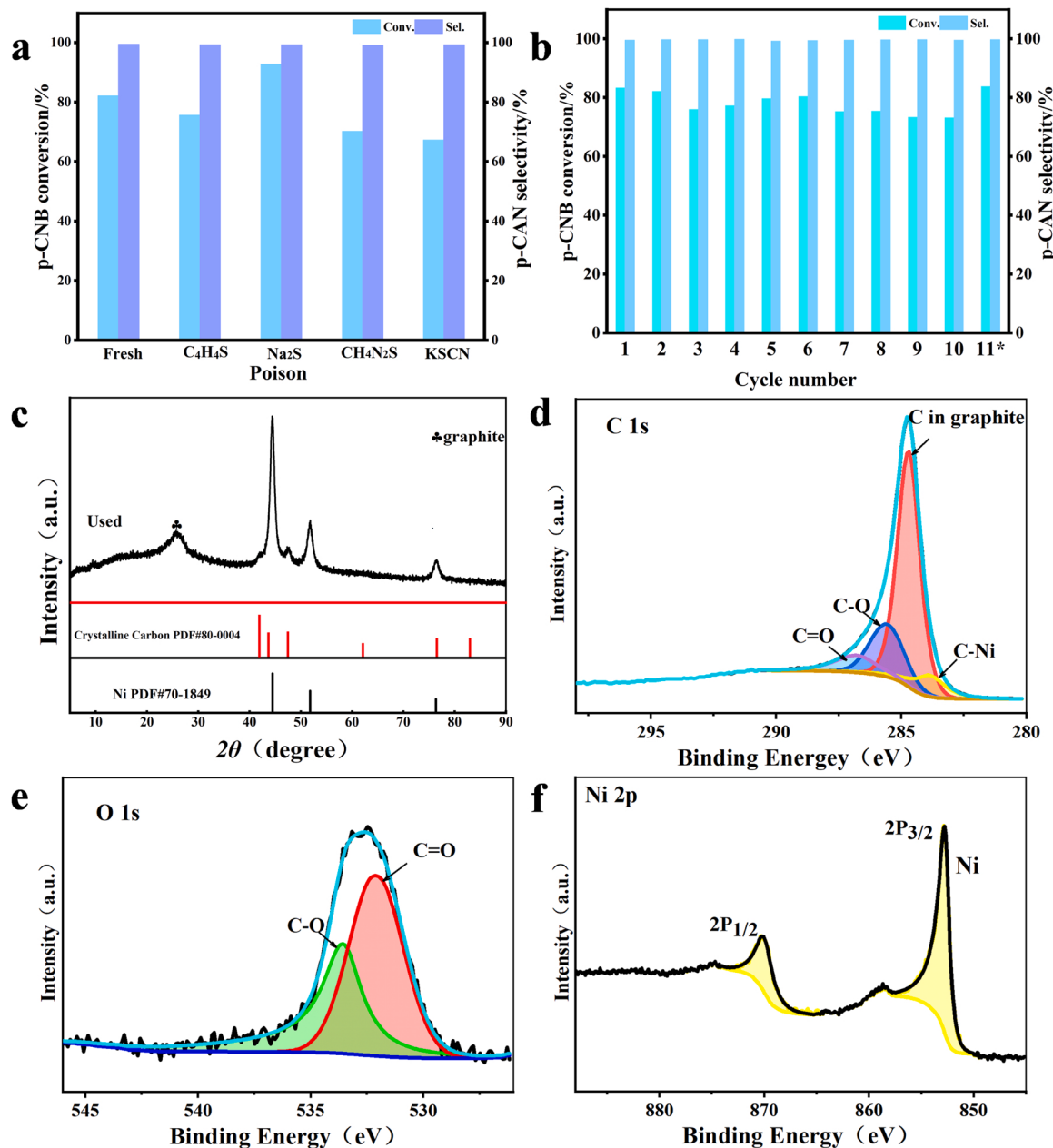


Fig. 7. (a) Comparison of the catalytic results of the hydrogenation of p-Chloronitrobenzene (p-CNB) in the presence or absence of Sulfur poisoning. Reaction conditions: p-CNB (0.2 g), catalyst (20 mg), methanol (25 mL), 1 MPa H_2 , 100 °C, 30 min, 0.1 g of poison; (b) Recyclability of the Ni@C-600 catalyst in the p-CNB. Reaction conditions: p-CNB (0.2 g), catalyst (20 mg), methanol (25 mL), 1 MPa H_2 , 100 °C, 30 min, * : the catalyst was treated with ultrasound 10 min before use, add 10% fresh catalyst before next use; (c) XRD patterns Ni@C-used (catalyst after 11 cycles). XPS spectra of Ni@C-used framework in (d) C 1s; (e) O 1s; (f) Ni 2p.

conditions, all sulfur-containing toxicants did not seriously damage the activity of the catalyst. Compared with the fresh catalyst, the selectivity and conversion rate of the poisoned catalyst could still be maintained. Even the addition of sodium sulfide, a reducing sulfur-containing toxicant, will increase the activity to a certain extent.

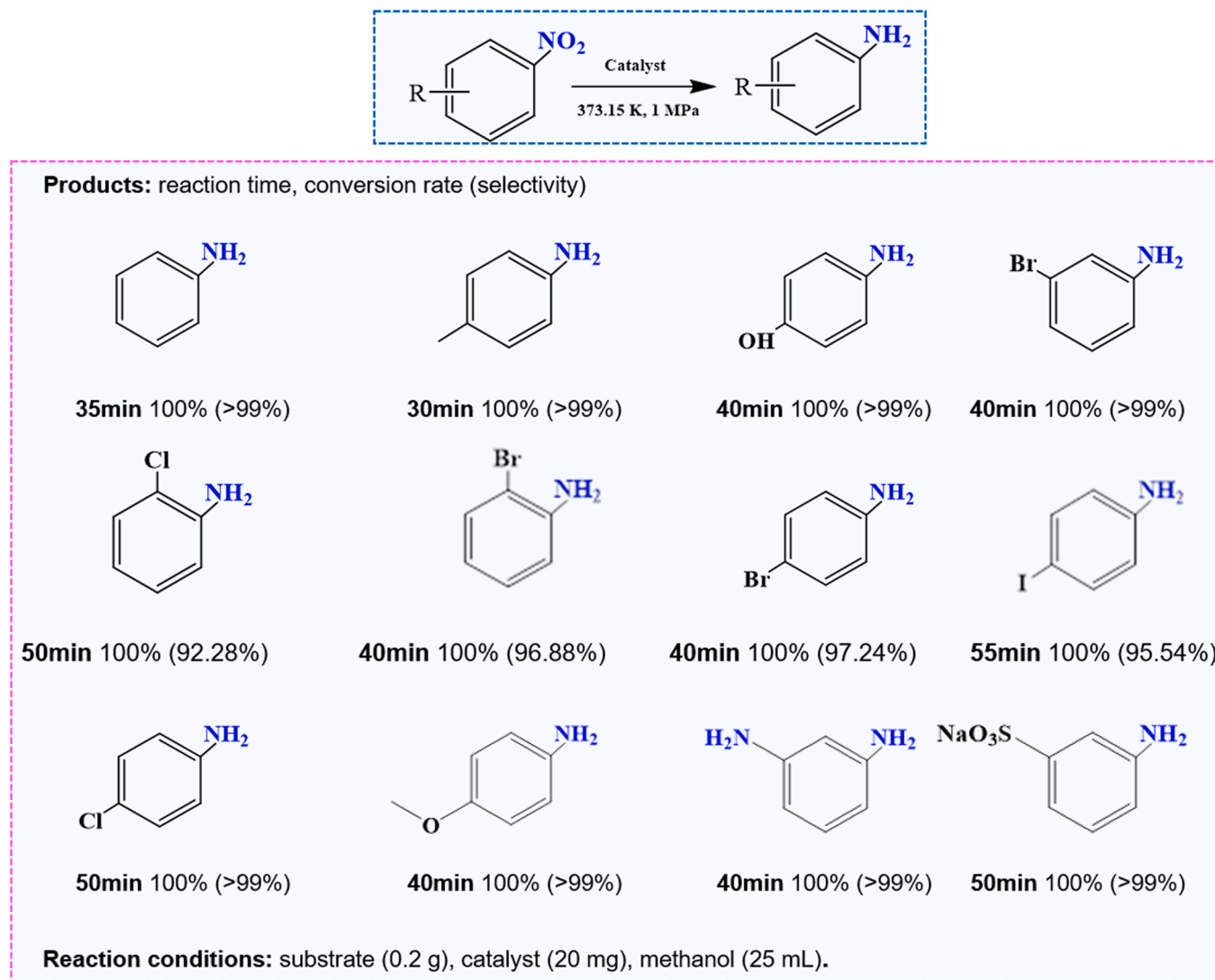
Easy separation and reusability of heterogeneous catalysts are essential properties for industrial applications[62,63]. In the experiment, the catalyst Ni@C-600 was able to separate from the reaction solution under an applied magnetic field (Fig. S5). In addition, we also carried out the Ni@C-600 cycle experiment still maintained its catalytic activity after 10 cycles, but the conversion rate of P-CNB decreased slightly, and the selectivity for P-CAN remained at a very high level (>99%). Before the 11th cycle experiment, the catalyst was subjected to ultrasonic treatment for 10 min to remove the physical adsorbed impurities on the surface. Therefore, the initial catalytic performance could still be maintained in the 11th cycle (Fig. 7b). At the same time, TEM, XRD, and XPS were used to verify the stability of the Ni@C-600 after 11 cycles. TEM images (Fig. S6) show that the encapsulated structure of the catalyst was not damaged. XRD analysis (Fig. 7c) shows that the phase composition of the catalyst was unchanged, and the characteristic diffraction peaks of nickel, graphitic carbon, and even crystalline carbon still exist. Compared with the XPS spectra of fresh catalysts, the Ni²⁺ disappeared in the Ni 2p spectrum and the Ni-O bond disappeared in the O 1s spectrum (Fig. 7e and f). The results show that the nickel oxide on

the surface of the catalyst was reduced to nickel metal by H₂ after 11 hydrogenation reactions. The status of the other species did not change (Fig. 7c and f), further demonstrating the excellent stability of the catalyst Ni@C-600.

Aromatic halo anilines are one of the most meaningful fine chemicals and organic intermediates[5,64,65]. Catalytic selective hydrogenation of halogenated nitrobenzene with H₂ as a reductant is considered to be the most environmentally friendly synthetic route of aromatic halo anilines[6,66,67]. To investigate the feasibility of the catalyst Ni@C-600 for the hydrogenation of nitroaromatic compounds, the selective hydrogenation reactions of various substituted nitroaromatic compounds (including Cl, Br, I, OH, CH₃, and other functional groups) were evaluated. As shown in Scheme 1, Ni@C-600 presented an excellent catalytic performance in hydrogenation, with high conversions (>99%) and selectivity (>90%). Notably, the yields of the corresponding aromatic amines reach as high as 90% or more under relatively mild reaction conditions. Dehalogenation was largely avoided in all cases.

4. Conclusions

In summary, a novel simple method has been constructed to prepare a multilayer graphite carbon layer encapsulated nickel core Ni@C-600 catalyst by pyrolyzing OCP precursor. It is revealed that the three major steps of catalyst growth during precursor pyrolysis include the



Scheme 1. Catalytic performance of Ni@C-600 in the hydrogenation of other nitroarenes.

decomposition of organic matter, reduction of Ni, and dissolution/segregation of carbon in the Ni nanoparticles. The directional selection of organic ligands could control the three stages of pyrolysis well. The catalyst Ni@C-600 prepared with succinic acid as the organic ligand has a smaller particle size and a larger curvature of the graphite-carbon layer. By kinetic research compared with the catalyst Ni@C-1 and DFT simulations, it could be found that a large curvature of the outer graphite-carbon layer in the catalyst Ni@C-600 could accept more electrons from the nickel core. Thus, a more optimized electronic structure was obtained and higher catalytic activity was contributed. In addition, Ni@C-600 has strong adaptability to the hydrogenation of nitroaromatic compounds. It could maintain a high nickel load after pickling, resisted a variety of sulfides, maintained catalytic performance after 11 cycles, and could be magnetic recovery.

CRediT authorship contribution statement

Xiaonian Li, Chunshan Lu, Yi Liu and Wei He initiated the idea and designed the experiments; Wei He, Jiaxin Yu and Xiyuan Zhang performed the experiments; Wei He, Yongyue Yao, Xin Liu, Chaofan Ma, Chunyu Yin, and Wei Yan analyzed the experiment data; Wei He, Chunshan Lu, Yi Liu, and Jiaxin Yu wrote the paper; All authors commented the manuscript.

Declaration of Competing Interest

The authors declare that they have no known competing financial interests or personal relationships that could have appeared to influence the work reported in this paper.

Data Availability

No data was used for the research described in the article.

Acknowledgments

This work was supported by the National Natural Science Foundation of China (No. 21978265, 22078302, and 22002140), the Joint Funds of the National Natural Science Foundation of China (No. U20A20119) and Zhejiang Provincial Natural Science Foundation of China under Grant (LR22B030003). Young Elite Scientist Sponsorship Program by CAST (NO. 2019QNRC001) was also acknowledged. Thank Shiyanjia lab (www.shiyanjia.com) for providing assistance in sample characterization.

Appendix A. Supporting information

Supplementary data associated with this article can be found in the online version at [doi:10.1016/j.apcatb.2023.122738](https://doi.org/10.1016/j.apcatb.2023.122738).

References

- [1] Jiajia Song, Zhen-Feng Huang, Lun Pan, Ke Li, Xiangwen Zhang, Li Wang, Ji-Jun Zou, Review on selective hydrogenation of nitroarene by catalytic, photocatalytic and electrocatalytic reactions, *Appl. Catal. B: Environ.* 227 (2018) 386–408.
- [2] Dario Formenti, Francesco Ferretti, Florian Korbinian Scharnagl, Matthias Beller, Reduction of nitro compounds using 3d-non-noble metal catalysts, *Chem. Rev.* 119 (2019) 2611–2680.
- [3] Xuejie Zhang, Yebin Zhou, Guowei Li, Lei Zhang, Chunyu Yin, Yuanyuan Yang, Hongzheng Wang, Feng Feng, Linwei Wei, Qunfeng Zhang, Feng Yang, Lili Lin, Chunshan Lu, Xiaonian Li, A highly sulfur resistant and stable heterogeneous catalyst for liquid-phase hydrogenation, *Appl. Catal. B: Environ.* 315 (2022) 121566.
- [4] Moritz Wolf, Ling Hui Wong, Christian Schüller, Olaf Hinrichsen, CO₂ methanation on transition-metal-promoted Ni-Al catalysts: sulfur poisoning and the role of CO₂ adsorption capacity for catalyst activity, *J. CO₂ Util.* 36 (2020) 276–287.
- [5] Zhijun Li, Mingyang Zhang, Xiuli Dong, Siqi Ji, Lili Zhang, Leipeng Leng, Honghong Li, J. Hugh Horton, Qian Xu, Junfa Zhu, Strong electronic interaction of indium oxide with palladium single atoms induced by quenching toward enhanced hydrogenation of nitrobenzene, *Appl. Catal. B: Environ.* 313 (2022), 121462.
- [6] Merce' Boronat, Patricia Concepcion, Avelino Corma, Silvia González Lez, Francesc Illas, P. Serna, A molecular mechanism for the chemoselective hydrogenation of substituted nitroaromatics with nanoparticles of gold on TiO₂ catalysts: a cooperative effect between gold and the support, *J. Am. Chem. Soc.* 129 (2007) 16230–16237.
- [7] Liang Wang, Erjia Guan, Jian Zhang, Junhao Yang, Yihan Zhu, Yu Han, Ming Yang, Cheng Cen, Gang Fu, Bruce C. Gates, Feng-Shou Xiao, Single-site catalyst promoters accelerate metal-catalyzed nitroarene hydrogenation, *Nat. Commun.* 9 (2018) 1362.
- [8] Chunshan Lu, Haoke Ji, Qianwen Zhu, Xuejie Zhang, Hao Wang, Yebin Zhou, Qiangqiang Liu, Juanjuan Nie, Juntao Ying, Xiaonian Li, Superior suppression hydrodehalogenation performance of Pd nanoparticle decorated with metalloid-promoter GQDs for the selective hydrogenation of halonitrobenzenes, *J. Mater. Sci.* 54 (2019) 10153–10167.
- [9] Yebin Zhou, Ling Li, Yi Liu, Hongzheng Wang, Zhenlong Feng, Feng Feng, Qunfeng Zhang, Wucan Liu, Wenfeng Han, Chunshan Lu, Xiaonian Li, Palladium nanoparticles inset into the carbon sphere with robust acid resistance for selective hydrogenation of chloronitrobenzene, *Ind. Eng. Chem. Res.* 61 (2022) 4310–4319.
- [10] Yu Wang, Ruixuan Qin, Yongke Wang, Juan Ren, Wenting Zhou, Laiyang Li, Jiang Ming, Wuyong Zhang, Gang Fu, Nanfeng Zheng, Chemoselective hydrogenation of nitroaromatics at the nanoscale Iron(III)-OH-platinum interface, *Angew. Chem. Int. Ed. Engl.* 59 (2020) 12736–12740.
- [11] Jiao Deng, Dehui Deng, Xinhe Bao, Robust catalyst on 2D materials encapsulating metals: concept, application, and perspective, *Adv. Mater.* 29 (2017).
- [12] Chuabo Gao, Fenglei Lyu, Yadong Yin, Encapsulated metal nanoparticles for catalysis, *Chem. Rev.* 121 (2021) 834–881.
- [13] Jiao Deng, Liang Yu, Dehui Deng, Xiaoqi Chen, Fan Yang, Xinhe Bao, Highly active reduction of oxygen on a FeCo alloy catalyst encapsulated in pod-like carbon nanotubes with fewer walls, *J. Mater. Chem. A* 1 (2013).
- [14] Jiao Deng, Pengju Ren, Dehui Deng, Xinhe Bao, Enhanced electron penetration through an ultrathin graphene layer for highly efficient catalysis of the hydrogen evolution reaction, *Angew. Chem. Int. Ed. Engl.* 54 (2015) 2100–2104.
- [15] Kailong Hu, Tatsuhiko Ohta, Linghan Chen, Jiuhan Han, Mitsuru Wakisaka, Yuki Nagata, Jun-ichi Fujita, Yoshikazu Ito, Graphene layer encapsulation of non-noble metal nanoparticles as acid-stable hydrogen evolution catalysts, *ACS Energy Lett.* 3 (2018) 1539–1544.
- [16] Jiaoshi Wang, Qinhong Wei, Qingxiang Ma, Zhongya Guo, Fangfang Qin, Zinfer R. Ismagilov, Wenzhong Shen, Constructing Co@N-doped graphene shell catalyst via Mott-Schottky effect for selective hydrogenation of 5-hydroxymethylfurfural, *Appl. Catal. B: Environ.* 263 (2020) 11839.
- [17] Xingxing Li, Yu Pan, Hong Yi, Jingcheng Hu, Dali Yang, Fengzhi Lv, Wendian Li, Jinping Zhou, Xiaojun Wu, Aiwen Lei, Lina Zhang, Mott-Schottky effect leads to alkynes semi-hydrogenation over Pd-nanocubes@N-doped carbon, *ACS Catal.* 5 (2019) 4632–4641.
- [18] Wei Yan, Fa-Zhan Xiao, Xin Li, Wei He, YongYue Yao, DongChuang Wan, Xin Liu, Yi Liu, Feng Feng, Qunfeng Zhang, Chunshan Lu, Xiaonian Li, Nickel and oxygen-containing functional groups co-decorated graphene-like shells as catalytic sites with excellent selective hydrogenation activity and robust stability, *Chem. Eng. J.* 452 (2023).
- [19] Iann C. Gerber, Philippe Serp, A theory/experience description of support effects in carbon-supported catalysts, *Chem. Rev.* 120 (2020) 1250–1349.
- [20] Fan Yang, Dehui Deng, Xulian Pan, Qiang Fu, Xinhe Bao, Understanding nano effects in catalysis, *Natl. Sci. Rev.* 2 (2015) 183–201.
- [21] S. Niyogi, M.A. Hamon, H. Hu, B. Zhao, P. Bhowmik, R. Sen, M.E. Itkis, R. C. Haddon, Chemistry of single-walled carbon nanotubes, *Acc. Chem. Res.* 35 (2002), 1105–1103.
- [22] Liang Yu, Dehui Deng, Xinhe Bao, Chain mail for catalysts, *Angew. Chem. Int. Ed. Engl.* 59 (2020) 15294–15297.
- [23] Dong Sung Choi, Chanhoon Kim, Joonwon Lim, Su-Ho Cho, Gil Yong Lee, Ho-Jin Lee, Jang Wook Choi, Heeyeon Kim, Il-Doo Kim, Sang Ouk Kim, Ultrastable graphene-encapsulated 3 nm nanoparticles by *in situ* chemical vapor deposition, *Adv. Mater.* 30 (2018), e1805023.
- [24] Eden Morales-Narváez, Lívia Florio Sgobbi, Sergio Antonio Spinola Machadob, Arben Merkoç, Graphene-encapsulated materials: synthesis, applications and trends, *Prog. Mater. Sci.* 86 (2017) 1–24.
- [25] Xiangru Wei, Mengyuan Zhou, Xiangcheng Zhang, Xiaoning Wang, Z. Wu, Applications of metal–organic framework-derived materials in fuel cells and metal-air batteries, *Coord. Chem. Rev.* 409 (2020), 213214.
- [26] Mohammad Yaser Masoomi, Ali Morsali, Applications of metal–organic coordination polymers as precursors for preparation of nano-materials, *Coord. Chem. Rev.* 256 (2012) 2921–2943.
- [27] Xiangru Wei, Mengyuan Zhou, Xiangcheng Zhang, Xiaoning Wang, Zhangxiong Wu, Amphiphilic mesoporous sandwich-structured catalysts for selective hydrogenation of 4-nitrostyrene in water, *ACS Appl. Mater. Interfaces* 11 (2019) 39116–39124.
- [28] Bhadra Biswa Nath, Ahmed Imteaz, Lee Hye Jin, Jhung Sung Hwa, Metal-organic frameworks bearing free carboxylic acids: preparation, modification, and applications, *Coord. Chem. Rev.* 450 (2022).
- [29] Lei Tong, Le-Le Zhang, Yu-Cheng Wang, Li-Yang Wan, Qiang-Qiang Yan, Cheng Hua, Chen-Jia Jiao, Zhi-You Zhou, Yan-Wei Ding, Bo Liu, Hai-Wei Liang, Hierarchically porous carbons derived from nonporous coordination polymers, *ACS Appl. Mater. Interfaces* 12 (2020) 25211–25220.
- [30] Kerstin Ledniowska, Hanna Nosal-Kovalenko, Weronika Janik, Agata Krasuska, Dorota Stańczyk, Ewa Sabura, Maria Bartoszewicz, Aleksandra Rybak, Effective,

environmentally friendly PVC plasticizers based on succinic acid, *Polym. (Basel)* 14 (2022).

[31] Lili Fitriani, Annisa Dezura Fitriandi, Uswatul Hasanah, Erizal Zaini, Nanocrystals of piperine-succinic acid: physicochemical characterization and dissolution rate studies, *ChemistrySelect* 7 (2022).

[32] Daiki Soma, Ren-Hua Jin, Biomimetic silica deposition promoted by sub-5 μ m complexes of dicarboxylic acids/polyethyleneimine microballs: a new approach to tuning silica structures using messenger-like dicarboxylic acids, *RSC Adv.* 8 (2018) 435–443.

[33] Shujun Chen, Xuejian Li, Jun Duan, Yue Fu, Zeyuan Wang, Min Zhu, Na Li, Investigation of highly efficient adsorbent based on Ni-MOF-74 in the separation of CO_2 from natural gas, *Chem. Eng. J.* 419 (2021), 129653.

[34] Xiaofei Wu, Zongbi Bao, Bin Yuan, Jun Wang, Yingqiang Sun, Hongmei Luo, Shuguang Deng, Microwave synthesis and characterization of MOF-74 (M=Ni, Mg) for gas separation, *Microporous Mesoporous Mater.* 180 (2013) 114–122.

[35] Hiroyoshi Ohtsu, Thomas D. Bennett, Tatsuhiko Kojima, David A. Keen, Yasuhiro Niwa, Masaki Kawanoa, Amorphous-amorphous transition in a porous coordination polymer, *Chem. Commun. (Camb.)* 53 (2017) 7060–7063.

[36] Ying Yang, Rijia Lin, Lei Ge, Lei Hou, Paul Bernhardt, Thomas E. Rufford, Shaobin Wang, Victor Rudolph, Yaoyu Wang, Zhonghua Zhu, Synthesis and characterization of three amino-functionalized metal-organic frameworks based on the 2-aminoterephthalic ligand, *Dalton Trans.* 44 (2015) 8190–8197.

[37] Yueling Cao, Shanjun Mao, Mingming Li, Yiqing Chen, Y. Wang, Metal/porous carbon composites for heterogeneous catalysis: old catalysts with improved performance promoted by N-doping, *ACS Catal.* 7 (2017) 8090–8112.

[38] Xinye Qian, Yuhe Wang, Lina Jin, Jian Cheng, Jianyu Chen, Bingbing Huang, Application of Ni-MOF derived Ni-C composite on separator modification for Li-S batteries, *J. Electroanal. Chem.* 907 (2022).

[39] R.D. Hunter, J. Ramírez-Rico, Z. Schnepp, Iron-catalyzed graphitization for the synthesis of nanostructured graphitic carbons, *J. Mater. Chem. A* 10 (2022) 4489–4516.

[40] Monika Sharma, Jue-Hyuk Jang, Dong Yun Shin, Jeong An Kwon, Dong-Hee Lim, Daeil Choi, Hukwang Sung, Jeonghee Jang, Sang-Young Lee, Kwan Young Lee, Hee-Young Park, Namgee Jung, Sung Jong Yoo, Work function-tailored graphene via transition metal encapsulation as a highly active and durable catalyst for the oxygen reduction reaction, *Energy Environ. Sci.* 12 (2019) 2200–2211.

[41] Zhengshuai Sun, Dingding Yao, Chengyao Cao, Zihang Zhang, Lili Zhang, Haodong Zhu, Qiaoxia Yuan, Baojun Yi, Preparation and formation mechanism of biomass-based graphite carbon catalyzed by iron nitrate under a low-temperature condition, *J. Environ. Manag.* 318 (2022), 115555.

[42] E. Thompson, A.E. Danks, L. Bourgeois, Z. Schnepp, Iron-catalyzed graphitization of biomass, *Green. Chem.* 17 (2015) 551–556.

[43] Yun Qiu, Ying Lin, Haibo Yang, Lei Wang, Mengqi Wang, Bo Wen, Hollow Ni/C microspheres derived from Ni-metal organic framework for electromagnetic wave absorption, *Chem. Eng. J.* 383 (2020).

[44] Aurora Gomez-Martin, Julian Martinez-Fernandez, Mirco Ruttert, Martin Winter, Tobias Placke, Joaquin Ramirez-Rico, Correlation of structure and performance of hard carbons as anodes for sodium ion batteries, *Chem. Mater.* 31 (2019) 7288–7299.

[45] A. Sadezky, H. Muckenhuber, H. Grothe, R. Niessner, U. Pöschl, Raman microspectroscopy of soot and related carbonaceous materials: spectral analysis and structural information, *Carbon* 43 (2005) 1731–1742.

[46] Changdong Sheng, Char structure characterised by Raman spectroscopy and its correlations with combustion reactivity, *Fuel* 86 (2007) 2316–2324.

[47] Dominique B. Schuepfer, Felix Badaczewski, Juan Manuel Guerra-Castro, Detlev M. Hofmann, Christian Heiliger, Bernd Smarsly, Peter J. Klar, Assessing the structural properties of graphitic and non-graphitic carbons by Raman spectroscopy, *Carbon* 161 (2020) 359–372.

[48] Hongqiang Li, Kaining Gan, Ran Li, Huawei Huang, Jiabao Niu, Zhipeng Chen, Jian Zhou, Yan Yu, Jieshan Qiu, Xiaojun He, Highly dispersed NiO clusters induced electron delocalization of $\text{Ni}[\square]\text{N}[\square]\text{C}$ catalysts for enhanced CO_2 electroreduction, *Adv. Funct. Mater.* 33 (2022).

[49] Enrico Lepre, Julian Heske, Michal Nowakowski, Ernesto Scoppola, Ivo Zizak, Tobias Heil, Thomas D. Kühne, Markus Antonietti, Nieves López-Salas, Josep Albero, Ni-based electrocatalysts for unconventional CO_2 reduction reaction to formic acid, *Nano Energy* 97 (2022).

[50] Zhe Wang, Chunpeng Wang, Shanjun Mao, Bing Lu, Yuzhuo Chen, Xie Zhang, Zhirong Chen, Yong Wang, Decoupling the electronic and geometric effects of Pt catalysts in selective hydrogenation reaction, *Nat. Commun.* 13 (2022) 3561.

[51] Liangmin Ning, Shengyun Liao, Hui Li, Ruoyan Tong, Caiqiao Dong, Mingtao Zhang, Wen Gu, Xin Liu, Carbon-based materials with tunable morphology confined Ni (0) and Ni-Nx active sites: highly efficient selective hydrogenation catalysts, *Carbon* 154 (2019) 48–57.

[52] Teng Chen, Siqi Guo, Jie Yang, Yida Xu, Jie Sun, Dali Wei, Zhaoxu Chen, Bin Zhao, Weiping Ding, Nitrogen-Doped Carbon Activated in Situ by Embedded Nickel through the Mott-Schottky effect for the oxygen reduction reaction, *ChemPhysChem* 18 (2017) 3454–3461.

[53] Yuan Huang, Haotong Yan, Chenyang Zhang, Yize Wang, Qinhong Wei, Renkun Zhang, Interfacial electronic effects in Co@N-doped carbon shells heterojunction catalyst for semi-hydrogenation of phenylacetylene, *Nanomaterials* 11 (2021).

[54] Hui Li, Hexing Li, Wei-Lin Dai, Weijiang Wang, Zhigang Fang, Jing-Fa Deng, XPS studies on surface electronic characteristics of Ni-B and Ni-P amorphous alloy and its correlation to their catalytic properties, *Appl. Surf. Sci.* 152 (1999) 25–34.

[55] Mark C. Biesinger, Brad P. Payne, Andrew P. Grosvenor, Leo W.M. Lau, Andrea R. Gerson, R.S.C. Smart, Resolving surface chemical states in XPS analysis of first row transition metals, oxides and hydroxides: Cr, Mn, Fe, Co and Ni, *Appl. Surf. Sci.* 257 (2011) 2717–2730.

[56] J.B. Burt, G.V. Gibbs, D.F. Cox, N.L. Ross, ELF isosurface maps for the Al₂SiO₅ polymorphs, *Phys. Chem. Miner.* 33 (2006) 138–144.

[57] Yongfang Sun, Yunlei Chen, Xiangyu Zhang, Yurong He, Zhongxian Qiu, Wentao Zheng, Fei Wang, Haijun Jiao, Yong Yang, Yongwang Li, Xiaodong Wen, The facile dissociation of carbon-oxygen bonds in CO_2 and CO on the surface of La₂SiH₆ intermetallic compound, *Angew. Chem. Int. Ed.* 60 (2021) 25538–25545.

[58] Yuke Bai, Yu Wu, Xichen Zhou, Yifan Ye, Kaiqi Nie, Jiaou Wang, Miao Xie, Zhixue Zhang, Zhaojun Liu, Tao Cheng, Chuanbo Gao, Promoting nickel oxidation state transitions in single-layer NiFeB hydroxide nanosheets for efficient oxygen evolution, *Nat. Commun.* 13 (2022) 6094.

[59] Si-Wen Zhang, Bo-Si Yin, Yong-Zheng Luo, Lei Shen, Bao-Shan Tang, Zongkui Kou, Xixia Liu, David-Boon-Kiang Lim, Da-Ming Gu, Zhen-Bo Wang, Hao Gong, Fabrication and theoretical investigation of cobaltosic sulfide nanosheets for flexible aqueous Zn/Co batteries, *Nano Energy* 68 (2020).

[60] Sibo Chen, Jihai Liao, Zining Zhou, Siyuan Yang, Qiongzhii Gao, Xin Cai, Feng Peng, Yueping Fang, Shengsen Zhang, Boosting photocatalytic hydrogen evolution using a noble-metal-free co-catalyst: CuNi@C with oxygen-containing functional groups, *Appl. Catal. B: Environ.* 291 (2021).

[61] Mo Zhang, Jing Guan, Yunchuan Tu, Shiming Chen, Yong Wang, Suheng Wang, Liang Yu, Chao Ma, Dehui Deng, X. Bao, Highly efficient H_2 production from H_2S via a robust graphene-encapsulated metal catalyst, *Energy Environ. Sci.* 13 (2020) 119–126.

[62] Tim Leshuk, Andrew B. Holmes, Duleeka Ranatunga, Paul Z. Chen, Yunsheng Jiang, Frank Gu, Magnetic flocculation for nanoparticle separation and catalyst recycling, *Environ. Sci.: Nano* 5 (2018) 509–519.

[63] Sujin Guo, Camilah D. Powell, Dino Villagrán, Michael S. Wong, Magnetic In–Pd catalysts for nitrate degradation, *Environ. Sci.: Nano* 7 (2020) 2681–2690.

[64] Ken-ichi Shimizu, Yuji Miyamoto, Atsushi Satsuma, Size- and support-dependent silver cluster catalysis for chemoselective hydrogenation of nitroaromatics, *J. Catal.* 270 (2010) 86–94.

[65] Qingshan Zhao, Wanxin Ni, Xiaojie Tan, Fengliang Cao, Tengfei Liu, Hao Huang, Zhinian Cheng, Yiwen Li, Shuwei He, Hui Ning, Wu Mingbo, A “Trojan horse” strategy towards robust Co–N₄ active sites accommodated in micropore defect-rich carbon nanosheets for boosting selective hydrogenation of nitroarenes, *J. Mater. Chem. A* 10 (2022) 9435–9444.

[66] Anne-Marie Alexander, J.S. Hargreaves, , Alternative catalytic materials: carbides, nitrides, phosphides and amorphous boron alloys, *Chem. Soc. Rev.* 39 (2010) 4388–4401.

[67] Rajenahally V. Jagadeesh, Annette-Enrica Sürküs, Henrik Junge, Marga-Martina Pohl, J.örg Radnik, Jabor Rabéah, Heming Huan, Volker Schünemann, Angelika Brückner, Matthias Beller, Nanoscale Fe_2O_3 -based catalysts for selective hydrogenation of nitroarenes to anilines, *Science* 342 (2013) 1073–1076.